Ongoing Global and Regional Adaptive Evolution of SARS-CoV-2

Nash D. Rochman[1,*], Yuri I. Wolf[1], Guilhem Faure[2], Pascal Mutz[1], Feng Zhang[2,3,4,5,6,*] and Eugene V. Koonin[1,*]

[1]National Center for Biotechnology Information, National Library of Medicine, Bethesda, MD 20894 [2]Broad Institute of MIT and Harvard, Cambridge, MA 02142; [3]Howard Hughes Medical Institute, Massachusetts Institute of Technology, Cambridge, MA 02139; [4]McGovern Institute for Brain Research, Massachusetts Institute of Technology, Cambridge, MA 02139; [5]Department of Brain and Cognitive Sciences, Massachusetts Institute of Technology, Cambridge, MA 02139; and [6]Department of Biological Engineering, Massachusetts Institute of Technology, Cambridge, MA 02139

For correspondence: nash.rochman@nih.gov, zhang@broadinstitute.org, koonin@ncbi.nlm.nih.gov

Keywords: SARS-Cov-2, phylogeny, ancestral reconstruction, epistasis, globalization

Abstract

Understanding the trends in SARS-CoV-2 evolution is paramount to control the COVID-19 pandemic. We analyzed more than 300,000 high quality genome sequences of SARS-CoV-2 variants available as of January 2021. The results show that the ongoing evolution of SARS-CoV-2 during the pandemic is characterized primarily by purifying selection, but a small set of sites appear to evolve under positive selection. The receptor-binding domain of the spike protein and the nuclear localization signal (NLS) associated region of the nucleocapsid protein are enriched with positively selected amino acid replacements. These replacements form a strongly connected network of apparent epistatic interactions and are signatures of major partitions in the SARS-CoV-2 phylogeny. Virus diversity within each geographic region has been steadily growing for the entirety of the pandemic, but analysis of the phylogenetic distances between pairs of regions reveals four distinct periods based on global partitioning of the tree and the emergence of key mutations. The initial period of rapid diversification into region-specific phylogenies that ended in February 2020 was followed by a major extinction event and global homogenization concomitant with the spread of D614G in the spike protein, ending in March 2020. The NLS associated variants across multiple partitions rose to global prominence in March-July, during a period of stasis in terms of inter-regional diversity. Finally, beginning July 2020, multiple mutations, some of which have since been demonstrated to enable antibody evasion, began to emerge associated with ongoing regional diversification, which might be indicative of speciation.

Significance

Understanding the ongoing evolution of SARS-CoV-2 is essential to control and ultimately end the pandemic. We analyzed more than 300,000 SARS-CoV-2 genomes available as of January 2021 and demonstrate adaptive evolution of the virus that affects, primarily, multiple sites in the spike and nucleocapsid protein. Selection appears to act on combinations of mutations in these and other SARS-CoV-2 genes. Evolution of the virus is accompanied by ongoing adaptive diversification within and between

geographic regions. This diversification could substantially prolong the pandemic and the vaccination campaign, in which variant-specific vaccines are likely to be required.

Introduction

High mutation rates of RNA viruses enable adaptation to hosts at a staggering pace (1-4). Nevertheless, robust sequence conservation indicates that purifying selection is the principal force shaping the evolution of virus populations, with positive selection affecting only relatively small subsets of sites directly involved in virus-host coevolution (5-8). The fate of a novel zoonotic virus is in part determined by the race between public health intervention and virus diversification. Even intermittent periods of positive selection can result in lasting immune evasion, leading to oscillations in the size of the susceptible population, and ultimately, a regular pattern of repeating epidemics, as has been amply demonstrated for Influenza(9-11).

During the current coronavirus pandemic (COVID-19), understanding the degree and dynamics of the diversification of severe acute respiratory syndrome coronavirus 2 (SARS-Cov-2) and identification of sites subject to positive selection are essential for establishing practicable, proportionate public health responses, from guidelines on isolation and quarantine to vaccination(12). To investigate the evolution of SARS-CoV-2, we collected all available SARS-Cov-2 genomes as of January 8, 2021, and constructed a global phylogenetic tree using a “divide and conquer” approach. Patterns of repeated mutations fixed along the tree were analyzed in order to identify the sites subject to positive selection. These sites form a network of potential epistatic interactions. Analysis of the putative adaptive mutations provides for the identification of signatures of evolutionary partitions of SARS-CoV-2. The dynamics of these partitions over the course of the pandemic reveals alternating periods of globalization and regional diversification.

Results and Discussion

Global multiple sequence alignment of the SARS-CoV-2 genomes

To investigate the evolution of SARS-CoV-2, we aggregated all available SARS-Cov-2 genomes as of January 8, 2021, from the three principal repositories: Genbank(13), Gisaid(14), and CNCB(15). From the total of 321,096 submissions in these databases, 175,857 unique SARS-Cov-2 genome sequences were identified, and 98,185 high quality sequences were incorporated into a global multisequence alignment (MSA) consisting of the concatenated open reading frames with stop codons trimmed. The vast majority of the sequences excluded from the MSA were removed due to a preponderance of ambiguous characters (see Methods). The sequences in the final MSA correspond to 175,776 isolates with associated date and location metadata.

Tree Construction

Several methods for coronavirus phylogenetic tree inference have been tested(16, 17). The construction of a single high-quality tree from nearly 200,000 30 kilobase (kb) sequences using any of the existing advanced methods is computationally prohibitive. Iterative construction of the complete phylogeny would seem an obvious solution such that a global topology would be obtained based on a subset of sequences available at an earlier date, and later sequences would be incorporated into the existing tree. However, this approach induces artifacts through the inheritance of deep topologies that differ substantially from any maximum-likelihood solution corresponding to the complete alignment.

Therefore, building on the available techniques, we utilized a “divide and conquer” approach which is not subject to these artifacts and furthermore can be employed for datasets that cannot be structured by sequencing date, including metagenomic analyses. This approach leverages two ideas. First, for any alignment, a diverse representative subset of sequences can be used to establish a deep topology, the tree “skeleton”, that corresponds to a maximum-likelihood solution over the entire alignment. Second, deep branches in an unrooted tree are primarily determined by common substitutions relative to consensus. In other words, rare substitutions are unlikely to

affect deep splits or branch lengths. We adopted the following steps to resolve the global phylogeny for SARS-CoV-2 (see Methods for details).

The first step is to construct sets of diverse representative sequences such that the topologies inferred from each subset share the same tree “skeleton” corresponding to that of the global topology. Sequence diversity is measured by the hamming distance between pairs of sequences; however, maximizing hamming distances among a set of representative sequences does not guarantee maximization of the tree distances in the resultant global topology and so does not guarantee the maximum-likelihood topology of this subset would share the global tree skeleton. Therefore, a reduced alignment containing only the top 5% of sites (ignoring nearly-invariant sites, see below) with the most common substitutions relative to consensus was constructed. Sequences redundant over this narrow alignment were removed. Sets of diverse, based on the hamming distances over this reduced alignment, representative sequences were then achieved and all subtrees generated from each diverse subset were aggregated to constrain a single, composite tree.

This composite tree reflects the correct tree skeleton and could be used to constrain the global topology; however, due to numerous sequencing errors in this dataset, another intermediate step was taken. A second reduced alignment was constructed in which nearly-invariant sites, which may represent sequencing errors and should not be used to infer tree topology, were omitted. As before, sequences redundant over this reduced alignment were removed and a tree was then constructed from this alignment, constrained to maintain the topology of the composite tree wherever possible. This tree reflects the correct topology of the global tree but has incorrect branch lengths. Finally, the global tree with the correct branch lengths (Fig. 1A) was constructed over the whole alignment, constrained to maintain the topology of previous tree wherever possible. A complete reconstruction of ancestral sequences was then performed by leveraging Fitch traceback(18), enabling comprehensive identification of nucleotide and amino acid replacements across the tree.

144 We identified 8 principal partitions within this tree, in a general agreement with other
145 work(19-21), along with three divergent clades (Fig. 1A) that, as discussed below, are
146 important for the interpretation of the metadata. Given the short evolutionary distances
147 between SARS-CoV-2 isolates, despite the efforts described above, the topology of the
148 global tree is a cause of legitimate concern(17, 22-24). For the analyses presented
149 below, we rely on a single, explicit tree topology which is probably one of many equally
150 likely estimates(17). Therefore, we sought to validate the robustness of the major
151 partitions of the virus genomes using a phylogeny-free approach. To this end, pairwise
152 Hamming distances were computed for all sequences in the MSA and the resulting
153 distance matrix was embedded in a 3-dimensional subspace using classical
154 multidimensional scaling. In this embedding, the 8 partitions are separated, and the
155 optimal clustering, determined by *k*-means, returned 5 categories (see Methods, Fig.
156 S1), of which 4 correspond to partitions 5 and 8, and the divergent clades v1 and v2.
157 These findings indicate that an alternative tree with a comparable likelihood but a
158 dramatically different coarse-grain topology, most likely, cannot be constructed from this
159 MSA.
160

161 **Mutational Signatures&Biases and Estimation of Selection**

162

163 Each of the 8 partitions and 3 variant clades can be characterized by a specific amino
164 acid replacement signature (Fig. 1B), generally, corresponding to the most prominent
165 amino acid replacements across the tree (Table S1), some of which are shared by two
166 or more partitions and appear independently many times, consistent with other
167 reports(25). The receptor binding domain (RBD) of the spike protein and a region of the
168 nucleocapsid protein associated with nuclear localization signals (NLS)(26) are enriched
169 with these signature replacements, but they are also found in the nonstructural proteins
170 1ab, 3a, and 8. The identification of these prevailing non-synonymous substitutions and
171 an additional set of frequent synonymous substitutions suggested that certain sites in
172 the SARS-CoV-2 genome might be evolving under positive selection. However,
173 uncovering the selective pressures affecting virus evolution was complicated by non-
174 negligible mutational biases. The distributions of the numbers of both synonymous and

175 non-synonymous substitutions across the genome were found to be substantially over-
176 dispersed compared to both the Poisson and normal expectations (Fig. S2).
177 Examination of the relative frequencies of all 12 possible nucleotide substitutions
178 indicated a significant genome-wide excess of C to U mutations, approximately
179 threefold higher than any other nucleotide substitution, with the exception of G to U, as
180 well as some region-specific trends. Specifically, G to U mutations increase steadily in
181 frequency throughout the second half of the genome and the distribution of nucleotide
182 substitutions over the polyprotein is dramatically different from other ORFs (Fig. S3).
183
184 Motivated by the observation of the mutational biases, we compared the trinucleotide
185 contexts of synonymous and non-synonymous substitutions as well as the contexts of
186 low and high frequency substitutions. The contexts of high-frequency events, both
187 synonymous and non-synonymous, were found to be dramatically different from the
188 background frequencies. The NCN context (that is, all C->D mutations) harbors
189 substantially more events than other contexts (all 16 NCN triplets are within the top 20
190 most high-frequency-biased, see Methods and Fig. S4) and is enriched in mutations
191 uniformly across the genome, primarily, among high-frequency sites. This pattern
192 suggests a mechanistic bias of the errors made by the coronavirus RNA-dependent
193 RNA polymerase (RdRP). Evidently, such a bias that increases the likelihood of
194 observing multiple, independent substitutions in the NCN context complicates the
195 detection of selection pressures. However, only 2 of the 9 contexts with an excess of
196 non-synonymous events are NCN (gct,tct, Fig. S4), suggesting that at least some of
197 these repeated, non-synonymous mutations are driven by other mechanisms. Thus, we
198 excluded all synonymous substitutions and non-synonymous substitutions with the NCN
199 context from further consideration in the determination of candidate sites evolving under
200 positive selection.
201
202 Beyond this specific context, the presence of any hypervariable sites complicates the
203 computation of the *dN/dS* ratio, the gauge of protein-level selection(27), which requires
204 enumerating the number of synonymous and non-synonymous substitutions within each
205 gene. Hypervariable sites bias this analysis, and therefore, we used two methods to

206 ensure reliable estimation of *dN/dS*. For each protein-coding gene of SARS-CoV-2
207 (splitting the long orf1ab into 15 constituent non-structural proteins), we obtained both a
208 maximum likelihood estimate of *dN/dS* across 10 sub-alignments and an approximation
209 computed from the global ancestral reconstruction (see Methods). This approach was
210 required due to the size of the alignment, which makes a global maximum likelihood
211 estimation computationally prohibitive. Despite considerable variability among the
212 genes, we obtained estimates of substantial purifying selection ($0.1<dN/dS<0.5$) across
213 most of the genome(Fig. S5), with a reasonable agreement between the two methods.
214 This estimate is compatible with previous demonstrations of purifying selection affecting
215 about 50% of the sites surveyed or more(5), among diverse RNA viruses(6).
216
217 **Evidence of Positive Selection**
218 As shown in the previous section, evolution of SARS-CoV-2 is likely primarily driven by
219 substantial purifying selection. However, more than 100 non-synonymous substitutions
220 appeared to have emerged multiple times, independently, covering a substantial portion
221 of the tree equivalent to approximately 200 or more terminal branches or “leaves”, and
222 were not subject to an overt mechanistic bias. Due to the existence of many equally
223 likely trees, in principle, in one or more of such trees, any of these mutations could
224 resolve to a single event. However, such a resolution would be at the cost of inducing
225 multiple parallel substitutions for other mutations, and thus, we conclude that more than
226 100 codons in the genome that are not subject to an overt mechanistic bias underwent
227 multiple parallel mutations in the course of SARS-CoV-2 evolution during the COVID-19
228 pandemic.
229
230 One immediate explanation of this observation is that these sites evolve under positive
231 selection. The possible alternatives could be that these sites are mutational hotspots or
232 that the appearance of multiple parallel mutations was caused by numerous
233 recombination events (either real or artifacts caused by incorrect genome assembly
234 from mixed infections) in the respective genomic regions. Contrary to what one would
235 expect under the hotspot scenario, we found that codons with many synonymous
236 substitutions tend to harbor few non-synonymous substitutions, and vice versa (Fig. S6

237 A). When a moving average with increasing window size was computed, only a weak
238 positive correlation was observed between the numbers of synonymous and non-
239 synonymous substitutions (Figs. S6 B&C, S7). Most sites in the virus genome are highly
240 conserved, the sites with most substitutions tend to reside in conserved neighborhoods,
241 and the local fraction of sites that harbor at least one mutation strongly correlates with
242 the moving average (Fig. S8). Together, these observations indicate that SARS-CoV-2
243 genomes are subject to diverse site-specific and regional selection pressures but we did
244 not detect regions of substantially elevated mutation or recombination in general
245 agreement with other studies(28) despite the role recombination might have played in
246 zoonosis(29-34).
247

248 ## Positively selected sites in SARS-CoV-2 proteins

249

250 Given the widespread purifying selection affecting evolving SARS-CoV-2 genomes,
251 substantially relaxed selection at any site is expected to permit multiple, parallel non-
252 synonymous mutations to the same degree that any site harbors multiple, parallel
253 synonymous mutations. Thus, seeking to identify sites subject to positive selection, we
254 focused only on those non-synonymous substitutions that independently occurred more
255 frequently than 90% of all synonymous substitutions excluding the mutagenic NCN
256 context (see Methods). Most if not all sites in the SARS-CoV-2 genome that we found to
257 harbor such frequent, parallel non-synonymous substitutions outside of the NCN context
258 can be inferred to evolve under positive selection (Table S2, List 1). The positively
259 selected residues form a co-occurrence network that likely reflects epistatic interactions
260 (Fig. 1D and Table S3, see Methods), in which the central hubs are D614G in the spike
261 (S) protein and two adjacent substitutions in the nucleocapsid (N) protein, R203K and
262 G204R, the three most common positively selected mutations (Fig. 1C) (35). Fig. 1D,).
263

264 **Positively selected amino acid replacements in the receptor-binding domain of**
265 **the spike protein**
266

267 Spike D614G appears to boost the infectivity of the virus, possibly, by increasing the
268 binding affinity between the spike protein and the cell surface receptor of SARS-CoV-2,
269 ACE2(36). Conclusively demonstrating selection for a single site has proven
270 challenging(37), even within this robust dataset. Although the emergence of this
271 mutation corresponds to the extinction of partitions lacking 614G (see below), the
272 possibility remains that this mutation is a passenger to some other mutagenic or
273 epidemiological event. The 614 site of the S protein is evolutionarily labile, so that the
274 ancestral reconstruction includes multiple gains of 614D after a previous loss. As a
275 result, the reverse replacement G614D appears often enough to pass our statistical
276 criteria for positive selection. Although severely biasing against recent events, one can
277 additionally require that the mean tree fraction descendant from each candidate
278 positively selected amino acid replacement be sufficiently large, removing from
279 consideration events which are frequent but shallow (see Methods). The addition of this
280 criterion results in a "shortlist" of 22 residues subject to the strongest selection (Table
281 S2, List 2) that do not include 614D.
282
283 Additionally, apart from the selective advantage of a single replacement, it should be
284 emphasized that D614G (but not G614D) is a central hub of the epistatic network (Fig.
285 1D). Conceivably, epistatic interactions with this residue can result in ensembles of
286 mutations which substantially increase fitness. The ubiquitous epistasis throughout
287 molecular evolution(38-41) suggests the possibility that many if not most mutations,
288 which confer a substantial selective advantage, do so only within a broader epistatic
289 context, not in isolation. By increasing the receptor affinity, D614G apparently opens up
290 new adaptive routes for later steps in the viral lifecycle. The specific mechanisms of
291 such hypothetical enhancement of virus reproduction remain to be investigated
292 experimentally.
293
294 In addition to 614G, 31 spike mutations, most within the RBD, are signature mutations
295 for divergent clades v1-3; emergent variants vAfrica or vOceania (see below); or
296 established variants B.1.1.7, B.1.1.7_E484K, B.1.258_delta, B.1.351, B.1.429, P.1, or
297 P.2(42-47) (Table S4, List 1). Three of these signature mutations pass the strict criteria

298 for positive selection: S|N501Y, S|S477N, and S|V1176F, and S|N501Y makes the
299 shortlist of the 22 strongest candidates. H69del/V70del are signature mutations for
300 variant B.1.258_delta and have been previously observed to have rapidly emerged in an
301 outbreak among minks(48, 49). A two amino acid deletion (in our alignment this deletion
302 resolves to sites 68/69 due to many ambiguous characters in this neighborhood)
303 appears multiple times independently throughout the tree and is present in
304 approximately one third of the European sequences from January, 2021(Fig. S9,
305 deletions are not shown in Fig. 1B, see below).
306
307 Two sites within the RBD, N331 and N343, have been shown to be important for the
308 maintenance of infectivity(50). As could be expected, these amino acid residues are
309 invariant. Four more substitutions in the RBD, among others, N234Q, L452R, A475V,
310 and V483A, have been demonstrated to confer antibody resistance(50). N234Q, A475V,
311 and V483A were never or rarely found in our alignment but L452R is a signature of
312 variant B.1.429. Although not meeting our criteria for positive selection, it appeared
313 multiple times across the tree, including within partition 1. Of greatest concern is
314 perhaps N501Y. This amino acid replacement is a signature of variants B.1.1.7,
315 B.1.1.7_E484K, B.1.351, P.1; divergent clade v2; and emergent variant vAfrica. N501Y
316 is among the 22 strongest candidates for positive selection and has been demonstrated
317 to escape neutralizing antibodies(51). N501T in the same site is of additional
318 concern(52) and has also been observed in mink populations(53). Additionally,
319 S|N439K, a signature mutation for variant B.1.258_DELTA that has been demonstrated
320 to enable immune escape(54), is observed in a large portion of the tree.
321
322 The emergence of multiple mutations associated with immune evasion during a period
323 of the pandemic when the majority of the global population had remained naïve is
324 striking. Such adaptations are generally expected to emerge among host populations
325 where many individuals have acquired immunity either through prior exposure or
326 vaccination(55-58). Furthermore, this pattern of, most likely independent, emergence of
327 persisting variants among both human and mink populations suggests the possibility
328 that these mutations represent non-specific adaptations acquired shortly after zoonosis.

329 The factors underpinning the evolution of viral life history traits after zoonosis, especially
330 virulence, remain poorly understood(59) but apparently result from selective pressures
331 imposed by both epidemiological parameters (host behavior)(60, 61), which may be
332 conserved across a variety of novel hosts, and specific properties of the host receptor.
333 Whereas emergent mutations in the RBD of SARS-CoV-2 are, for obvious reasons,
334 surveyed with great intensity, we have to emphasize the enrichment of positively
335 selected residues in the N protein, which might relate to more deeply taxonomically
336 conserved routes of host adaptation for beta-coronaviruses.
337

338 **Amino acid replacements associated with the nuclear localization signals in the**
339 **nucleocapsid protein**

340

341 Evolution of beta-coronaviruses with high case fatality rates including SARS-CoV-2 was
342 accompanied by accumulation of positive charges in the N protein that might enhance
343 its transport to the nucleus(62). Thirteen amino acid replacements in the N protein are
344 signatures among the variants or major partitions discussed here, 7 of which: 203K,
345 204R, 205I, 206F, 220V, 234I, and 235F, are in the vicinity of the known NLS motifs or
346 other regions responsible for nuclear shuttling(26). Two additional substitutions, 194L
347 and 199L, rose to prominence in multiple regions during the summer of 2020. Two of
348 these NLS-adjacent amino acid replacements, R(agg)203K(aaa) and G(gga)204R(cga),
349 almost always appear together. This pair of substitutions includes the second and third
350 most common positively selected sites after S614, and although another adjacent site,
351 S(agt)202N(aat) is not a signature mutation, it is the 8th most common positively
352 selected residue. Among the 22 nonsynonymous substitutions that are apparently
353 subject to the strongest selection (Table S2, List 2), 6 are in the N protein (202N, 203K,
354 204R, 234I, 292T, and 376T).
355

356 The replacements R(agg)203K(aaa) and G(gga)204R(cga) occur via three adjacent
357 nucleotide substitutions. R(agg)203K(aaa) resolves to two independent mutations in the
358 ancestral reconstruction: first, R(agg)203K(aag), then K(aag)203K(aaa). Furthermore,
359 the rapid rise of 220V (excluded from consideration as a candidate for positive selection

360 in our analysis due to its NCN context) in a European cohort during the summer of 2020
361 might be related to a transmission advantage of the variant carrying this
362 substitution(63).These substitutions, in particular G(gga)204R(cga), which increases the
363 positive charge, might contribute to the nuclear localization of the N protein as well. This
364 highly unusual cluster of multiple signature and positively selected mutations across 5
365 adjacent residues in the N protein is a strong candidate for experimental study that
366 could illuminate the evolution and perhaps the mechanisms of SARS-CoV-2
367 pathogenicity.
368
369 In addition to the many mutations of interest in the N and S proteins, Orf3a|Q57H is a
370 signature mutation for partitions 6, 7, and v1. Q57H is the 4th most common positively
371 selected mutation. Although not considered a candidate for positive selection in our
372 analysis due to its NCN context, ORF8 S84L is a hub in the larger epistatic network
373 including all strongly associated residues (Fig. S10).
374
375 We also identified numerous nonsense mutations. Of particular interest seems to be
376 ORF8|Q27*, which is a signature for variants B.1.1.7 and B.1.1.7_E484K and could be
377 epistatically linked to positively selected residues including N|R203K and S|D614G.
378 ORF8 has been implicated in the modulation of host immunity by SARS-CoV-2, so
379 these truncations might play a role in immune evasion(64, 65).
380
381 **Potential role of epistasis in the evolution of SARS-CoV-2**
382
383 Epistasis in RNA virus evolution, as demonstrated for influenza, can constrain the
384 evolutionary landscape and promote compensatory variation in coupled sites, providing
385 an adaptive advantage which would otherwise impose a prohibitive fitness cost(66-68).
386 Because even sites subject to purifying selection can play an adaptive role through
387 interactions with other residues in the epistatic network(69), the networks presented
388 here (Figs. 1D, S10) likely underrepresent the extent of epistatic interactions occurring
389 during SARS-CoV-2 evolution. The early evolutionary events that shaped the epistatic
390 network likely laid the foundation for the diversification of the virus relevant to virulence,

391 immune evasion, and transmission. As discussed above, these early mutations
392 (including S|G614D) might provide only a modest selective advantage in isolation but
393 exert a much greater effect through multiple epistatic interactions.
394
395 The epistatic network will continue to evolve through the entirety of the pandemic, and
396 indeed, all emerging variants at the time of this writing are defined not by a single
397 mutation but by an ensemble of signature mutations. Moreover, in addition to the
398 apparent widespread intra-protein epistasis, there seem to exist multiple epistatic
399 interactions between the N and S proteins. In particular, S|N501Y and N|S235F are both
400 signature mutations for variants B.1.1.7 and B.1.1.7_E484K (Table S4, List 2) and this
401 pair is in the top 25% of co-occurring pairs in our network ranked by lowest probability of
402 random co-occurrence.
403
404 As with early founder mutations, when a new variant emerges with multiple signature
405 mutations, it is unclear which, if any, confer a fitness advantage. Although it is natural to
406 focus on substitutions within the RBD, we emphasize that all emergent variants contain
407 substitutions in in the vicinity of known NLS motifs. In fact, the most statistically
408 significant signature mutation (based on the Kullback-Leibler divergence) for vAfrica
409 (consistent with variant B.1.351, see below) is N|T205I. As we suggest for S|D614G,
410 these variant signature mutations are likely to exert a greater influence through multiple
411 epistatic interactions than in isolation and each signature mutation can be a member of
412 multiple epistatic ensembles beyond the group of signature mutations within which it
413 was originally identified. Indeed signature mutations are shared among defined variants
414 and we find evidence for an additional 18 putative epistatic interactions between variant
415 signature mutations and other events throughout the tree which are not identified as
416 signature mutations for any defined variant (Table S4, List 3). The growing ensemble of
417 signature mutations that appear to be subject to positive selection and the existence of
418 a robust network of putative epistatic interactions including these signatures, suggest
419 that ongoing virus diversification is driven by host adaptation rather than occurring
420 simply by neutral drift.
421

Epidemiological Trends and Ongoing Diversification of SARS-CoV-2

Analysis of within-patient genetic diversity of SARS-CoV-2 has shown that the most common mutations are highly diverse within individuals(70-72). Such diversity could either result from multiple infections, or otherwise, could point to an even greater role of positive selection affecting a larger number of sites than inferred from our tree. Similarly to the case of Influenza, positive selection on these sites could drive virus diversification and might support a regular pattern of repeat epidemics, with grave implications for public health. An analysis of the relationships between the sequencing date and location of each isolate and its position within the tree can determine whether diversification is already apparent within the evolutionary history of SARS-CoV-2.

We first demonstrated a strong correlation between the sequencing date of SARS-CoV-2 genomes and the distance to the tree root (Fig. S11), indicating a sufficiently low level of noise in the data for subsequent analyses. Examination of the global distribution of each of the major SARS-CoV-2 partitions (Figs. S12-14) indicates dramatic regional differences and distinct temporal dynamics (Fig. 2). A measure of virus diversity is necessary to map to these trends. We considered two modes of diversity. Intra-regional diversity reflects the mutational repertoire of the virus circulating in any individual region within any window of time. To measure intra-regional diversity, we sampled pairs of isolates from each region and timepoint and computed the mean tree-distance for a representative ensemble of these pairs. We found that intra-regional diversity has been steadily increasing throughout the entirety of the pandemic, with the exception of Oceania from June-August, 2020 (Figs. 3A/B) which corresponds to the period following a bottleneck in the total number of infections (Fig. S15) within that region. This unabated intra-regional diversification is a further evidence of a large repertoire of host-adaptive mutations of SARS-CoV-2 evolving within the human population.

The inter-regional diversity measures the degree to which the virus can be categorized into region-specific subtypes. A demonstration of substantial inter-regional diversity would perhaps constitute the most compelling and concerning evidence of the potential

453 for repeat epidemics. We developed two measures of inter-regional diversity. The first
454 one is analogous to the intra-regional diversity measure. We sampled pairs of isolates
455 within each region and between each pair of regions within the same time window,
456 computed the mean tree-distance for both representative ensembles of these pairs
457 (intra- and inter-regional pairs), and calculated the ratio of inter-regional and intra-
458 regional values (Fig. S16). The second one is a partition-level measure. For every pair
459 of regions over each time window, we computed the Hellinger distance of the 11-group
460 frequency distribution between all pairs of regions over each time window. (See
461 Methods for details).
462
463 Both measures of inter-regional diversity support the division of the pandemic, through
464 the beginning of 2021, into four periods (Fig1. 3C). The first period that ended in
465 February 2020 represents rapid diversification into region-specific phylogenies. This
466 period was followed by a major extinction event and global homogenization ending in
467 March 2020. The following five months, March-July, represented a period of stasis, in
468 terms of inter-regional diversity. Finally, July 2020 was the start of the ongoing period of
469 inter-regional diversification.
470
471 The extinction of the earliest partitions, 1 and 2, corresponds to the advent of S|D614G,
472 which became fixed in all other partitions and was globally ubiquitous by June 2020
473 (Fig. 3D). Partition 8, the only partition where N|203K and 204R were fixed, became
474 dominant in every region outside of North America in the period that followed (Fig. S17).
475 However, this did not result in a global selective sweep that would involve the extinction
476 of partitions 1-7. Instead, multiple NLS-associated mutations rose to prominence across
477 different partitions, becoming globally dominant by September (Figs. 3D, S18). To
478 resolve this trend, at least two principal variants, N|203K/204R in partition 8 and N|220V
479 in partition 5, have to be considered, and we identified 6 key amino acid replacements
480 of interest for this period (N|203K/204R, N|220V, N|199L, N|194L, N205I, N206F).
481
482 In the next phase of the pandemic, partition 8 dramatically fell from dominance in two
483 regions, Africa and Oceania, replaced by partitions 6 and 7. Although we did not find a

484 distinct mutational signature associated with the rise of partition 7 in Oceania (Fig. S19),
485 signatures associated with the rise of partition 6 were identified in both regions (Figs.
486 S20-21). Neither of these two groups of sequences (late sequences from partition 6,
487 Oceania and Africa, respectively) form topologically distinct clades; however, due to the
488 conserved mutational signatures, we considered both groups to represent distinct
489 emerging variants, vOceania and vAfrica. The signature for vAfrica is consistent with
490 variant B.1.351. Additionally, two divergent clades within partition 8 and one clade within
491 partition 3 emerged.
492
493 The most prominent is clade v2 with a signature consistent with variant B.1.1.7.
494 Altogether, resolving this trend of emerging substitutions in the RBD (Figs. 3D, S22-24)
495 requires the consideration of at least 3 variants and includes 59 signature mutations.
496 Clade v1 appeared first in Europe in April, 2020, v2, also in Europe, in September,
497 2020, and V3 in Asia and North America, in April, 2020 (Fig. S25). Also notably,
498 although S|477N initially appears in February/March, 2020 in Europe, Oceania, and
499 North America, it dramatically rises to prominence in Oceania in April, about 3 months
500 before this mutation becomes prominent elsewhere. S|477N is a signature mutation for
501 v1 stemming from partition 3; however, the sequences from Oceania bearing this
502 mutation from Summer, 2020 are in partition 8. The dramatic diversity of signature
503 mutations among these variants decreases the likelihood of future selective sweeps (in
504 the absence of bottlenecks in the total number of infected hosts) and increases the
505 likelihood of repeat epidemics.
506
507 **The impact of SARS-CoV-2 Diversification on Testing and Vaccination**
508
509 The ongoing diversification of SARS-CoV2 poses problems for both testing and
510 vaccination. Substitutions in the E protein have already been demonstrated to interfere
511 with a common PCR assay(73). Generally, ORF1ab is more conserved than the S
512 protein, which itself is more conserved than the remaining ORFs (Figs. S2-3). Using our
513 SARS-CoV-2 MSA, we surveyed 10 regions from ORF1ab(5), N(4), and E(1) genes that
514 are commonly used in PCR assays(74) for substitutions relative to the reference

515 sequence. Among the more than 175k genome sequences, there were thousands of
516 nucleotide substitutions in each of these regions, but those in ORF1ab were markedly
517 less variable than those in N (Supplementary table 5), with one region in N
518 demonstrating variability in nearly one third of all isolates. It can be expected that most
519 targets within the polyprotein will remain subject to the fewest polymorphism-induced
520 false negatives even as the virus continues to diversify.
521
522 Of the 9 primary vaccines/candidates (75), three are inactivated whole-virus (Sinovac,
523 Wuhan Institute of Biological Products/Sinopharm, Beijing Institute of Biological
524 Products/Sinopharm); five utilize the entire spike protein as the antigen
525 (Moderna/NIAID, CanSino Biological Inc./Beijing Institute of Biotechnology, University of
526 Oxford/AstraZeneca, Gamaleya Research Institute, Janssen Pharmaceutical
527 Companies) and one utilizes only the RBD (Pfizer/Fosun Pharma/BioNTech). In addition
528 to the greater sequence conservation of the spike protein relative to all other ORFs
529 outside of the polyprotein, it is the principal host-interacting protein of SARS-CoV-2,
530 making both the whole protein and the RBD obvious antigenic candidates. Most
531 mutations in the RBD were demonstrated to decrease infectivity, but some conferred
532 resistance to neutralizing antibodies(49). Multiple mutations in the RBD are signature
533 mutations in emerging variants and some have been demonstrated to result in
534 neutralizing antibody evasion(51). Different choices of the antigen could result in more
535 or less generalizable immunity to these variants.
536

537 ## Conclusions

538 Virus evolution during a pandemic is a fast moving target, and unavoidably, aspects of
539 this analysis will be outdated by the time of publication. Nevertheless, several trends
540 revealed here appear general and robust. Although it is difficult to ascertain positive
541 selection for individual sites, the overall adaptive character of SARS-CoV-2 evolution
542 involving multiple amino acid replacements appears to be beyond reasonable doubt. As
543 expected, there are multiple positively selected sites in the S protein, but more
544 surprisingly, N protein includes several sites that appear to be strongly selected as well.
545 The involvement of these adaptive substitutions in the nuclear localization of the N

protein appears likely. Importantly, some of the mutations, for which positive selection was inferred, co-occur on multiple occasions and seem to form a robust epistatic network. Most likely, the effect of positive selection is manifested primarily at the level of epistatic interactions.

Clearly, despite the dramatic reduction of global travel(76), the evolution of SARS-Cov-2 is partly shaped by globalizing factors, including the increased virus fitness conferred by S|D614G, N|R203K&G204R, and other positively selected substitutions. However, we obtained strong evidence of both continuous virus diversification within geographic regions and “speciation”, that is, formation of stable, diverging region-specific variants. This ongoing adaptive diversification could substantially prolong the pandemic and the vaccination campaign, in which variant-specific vaccines are likely to be required.

Author contributions

EVK initiated the project; NDR and GF collected data; NDR, GF, YIW, PM, FZ and EVK analyzed data; NDR and EVK wrote the manuscript that was edited and approved by all authors.

Acknowledgements

The authors thank Koonin group members for helpful discussions. NDR, YIW PM, and EVK are supported by the Intramural Research Program of the National Institutes of Health (National Library of Medicine).

Methods

Multiple alignment of SARS-CoV-2 genomes

All available SARS-CoV-2 genomes as of January 8, 2021 were retrieved from the Genbank(13), Gisaid(14), and CNCB(15) datasets. Sequences with apparent anomalies (sequence inversion etc.) were immediately discarded. Sequences were harmonized to DNA (e.g. U was transformed to T to amend software compatibility) and clustered according to 100% identity with no coverage threshold using CD-HIT(77, 78), with ambiguous characters masked. All characters excepting ACGT were considered ambiguous. The least ambiguous sequence from each cluster was selected and sequences shorter than 25120 nucleotides were discarded.

Exterior ambiguous characters (preceding/succeeding the first/last defined nucleotide) were removed, and sequences with more than 10 remaining interior, ambiguous characters were discarded. A reference alignment was previously constructed using the same protocol as follows with the exception of the --keeplength specification in November, 2020. The updated database was aligned using multi-threaded MAFFT(79) with 80 cores (--thread 80, when more cores were allocated they were not utilized) and 3.8Tb of RAM to maintain usage of the normal DP algorithm(79) (--nomemsave) against this reference alignment (specifying --keeplength). Aligning “from scratch” without --keeplength proved to be prohibitively slow so we recommend first constructing a reference alignment from a suitable subset of sequences. Sequences sourced from non-human hosts were manually identified from the metadata and those excluded at the previous step were added to the alignment using MAFFT, (again specifying --keeplength). Note that use of the --keeplength option will not include insertions relative to the reference alignment.

Sites corresponding to protein-coding ORFs were then mapped to the alignment from the reference sequence NC_045512.2 excluding stop codons as follows: 266-13468+13468-21552, orf1ab; 21563-25381, S; 25393-26217, orf3a; 26245-26469, E; 26523-27188, M; 27202-27384, orf6; 27394-27756, orf7a; 27756-27884, orf7b; 27894-28256, orf8; and 28274-29530, N. The remaining sites were discarded.

The resulting alignment contained out-of-frame gaps. Gaps in the reference sequence, corresponding to insertions, were found to correspond to gaps in all but fewer than 1% of the remaining sequences (all gaps in the reference sequence correspond to gaps in the alignment from November, 2020, the use of --keeplength prohibited the recognition of any insertions relative to the reference sequence which were not present in this reference alignment). These sites were discarded. The remaining gaps, corresponding

605 to deletions relative to the reference sequence, shorter than three nucleotides were
606 replaced with the ambiguous character, N. Longer gaps were shifted into frame and
607 padded with ambiguous characters on either end of the gap, minimizing the number of
608 sites altered.

609 A fast, approximate tree was then built using FastTree(80) (parameters: -nt -gtr -gamma
610 -nosupport -fastest) to unambiguously define two clusters of sequences: an outgroup
611 consisting of 14 sequences sourced from non-human hosts prior to 2020 and the main
612 group. The tree construction requires the resolution of very short branch lengths which
613 makes it necessary to compile FastTree at double precision. Outliers from the remaining
614 sequences were then identified based on the Hamming distance (excluding gaps and
615 ambiguous characters) to the nearest neighbor, the Hamming distance to the
616 consensus, and the degree to which those substitutions relative to consensus were
617 clustered in the genome. At this step, 81 sequences were removed.

618 The resulting alignment, consisting of 98,185 sequences and 29,119 sites, was
619 maintained for the construction of the global tree and ancestral sequence
620 reconstruction. In an effort to minimize the impact of sequencing error on the tree
621 topology, as well as to decrease computational costs, a reduced alignment was then
622 constructed through the removal of 1) invariant sites, 2) sites invariant with the
623 exception of a single sequence, and 3) sites invariant throughout the main group with
624 the exception of at most one sequence representing each minority nucleotide.
625 Removing these sites created substantial redundancy, so a representative sequence
626 was selected for each cluster of 100% identity to yield an alignment consisting of 90,585
627 sequences and 16,487 sites. As described below and in the main text, a third alignment
628 was constructed including only the top 5% of sites with the most common substitutions
629 relative to consensus (of this second alignment) and again removing redundant
630 sequences to yield 32,563 sequences and 834 sites.

631

632 ## Tree Construction

633 We sought to optimize tree topology with IQ-TREE(81); however, building the global
634 tree was computationally prohibitive, and thus, we proceeded to subsample the smallest
635 alignment (834 sites) as follows. First, a core set of maximally diverse sequences is
636 selected. The set is initialized with a pair of sequences: a sequence maximizing the
637 number of substitutions relative to consensus and a paired sequence which maximizes
638 the Hamming distance to itself. Sequences are then added to this core set one at a time
639 maximizing the minimum Hamming distance to any representative of the set until *N*
640 sequences are incorporated. Next, $ceil\big(L/(M-N)\big)$ resulting sets are initialized with this
641 core set where *M* is the target number of sequences and *L* is the total number of
642 sequences in the alignment (32,363). Then, sequences that have not yet been
643 incorporated into any resulting set are added to each resulting set, again one at a time,
644 maximizing the minimum distance to any representative of the set until *M* sequences

are incorporated. The order of the resulting sets is randomized at each iteration without repeats. Once every (main group) sequence has been incorporated into at least one resulting set, sequences are randomly incorporated into each set until every set contains *M* sequences. Finally, the outgroup is added to each resulting set. We chose *M*=3,000 in an effort to optimize computational efficiency and *N*=300. Note that while increasing *N* increases the number of sets required for alignment coverage, and thus compute time, insufficient overlap between the sequences assigned each sub-alignment greatly affects the results of subsequent steps. As discussed in the main text, executing this protocol on an alignment containing most or all sites may not yield a consistent deep tree topology or "skeleton" since maximizing the hamming distance of any subset over all sites does not guarantee maximizing the tree distance in the resultant global topology. This is why limiting the alignment to sites with common substitutions relative to consensus is essential at this step.

A tree was then built, using IQ-TREE, for each maximally diverse set, with the evolutionary model fixed to GTR+F+G4 and the minimum branch length decreased from the default 10e-6 to 10e-7, according to the results of previous parameter studies(17). These trees were then converted into constraint files and merged to generate a single global constraint file for use within FastTree (parameters: -nt -gtr -gamma -cat 4 -nosupport -constraints).

The remaining sequences excluded from this tree but present in the second alignment (90,585 sequences and 16,487 sites) were then reintroduced as unresolved multifurcations and a new constraint file from the multifurcated tree was constructed. A second iteration of FastTree was initiated on the second alignment to produce an intermediate tree. This tree was primarily constructed as an intermediate step to limit the impact of sequencing errors on the final topology as mentioned in the main text; however, it is also less computationally intensive. The last step was then repeated on this intermediate tree to construct the global topology for the whole alignment. The final, global tree was rooted at the outgroup.

Reconstruction of Ancestral Genome Sequences

Ancestral states were estimated by Fitch Traceback(18). Briefly, character sets were constructed from leaf to root where each node was assigned the intersection of the descendant character sets if not empty and the union otherwise. Then, moving from root to leaf, nodes with more than one character in their set were assigned the consensus character if present in their set or a randomly chosen representative character otherwise. Substitutions between states were identified and placed in the middle of the branch bridging the pair of nodes.

Statistical associations between mutations were computed in a manner similar to that previously described(35). Briefly, sequences were leaf-weighted based on the branch lengths of the ultrameterized, tree. Every mutation present across the tree at 200 mean

leaf-weight equivalents or more was considered. The probability of independent co-occurrence between any pair was estimated in two ways. An arbitrary member of the pair was selected as the ancestral mutation, and the binomial probability:

$$\sum_{k=N_{pair}}^{N_{total}} \binom{N_{total}}{k} F^k (1-F)^{N_{total}-k}$$

was computed where *N_total* is the number of substitutions to the descendant mutation across the entire ancestral record, *N_pair* is the number of substitutions to the descendant which succeed or appear simultaneously with a substitution to the ancestral mutation, and *F* is the fraction of the tree (fraction of all applicable branch lengths) occupied by the ancestral mutation. The ancestral/descendent designation was then reversed and the "binomial score" was constructed as the negative log of the product of these two terms. Additionally, for each pair, the observed and expected (product of the tree fractions) tree intersections were calculated and the "Poisson score" (analogous to the log-odds ratio) was calculated:

$$\begin{cases} -\ln\big(1 - PCDF(exp, obs)\big), obs > exp \\ \ln\big(PCDF(exp, obs)\big), obs < exp \end{cases}$$

where PCDF(exp,obs) is the cumulative probability of a Poisson distribution with mean "exp", the expected value of the data, and evaluated at "obs", the observed value of the data. Both scores are reported. Table S3 displays putative positively selected mutations with both scores above 5 or at least two simultaneous substitutions. Fig. 1D only displays associations between mutations in the N or S proteins. Fig. S10 does not exclude mutations with NCN context but meets all other statistical criteria for positive selection and does not display mutations in the polyprotein.

Classical Multidimensional Scaling of the MSA

Pairwise Hamming distances were computed for all pairs of rows in the global MSA ignoring gaps and ambiguous characters i.e. the sequences *X*="ATN-A" and *Y*="NTAAT" would be assigned a distance of 1. The resulting distance matrix was embedded in three dimensions with the MATLAB(82) routine "cmdscale". 100 rounds of stochastically initiated k-means clustering of the embedding was conducted and the optimum cluster number was determined to be 5 on the basis of the silhouette score distribution (Fig S1).

Validation of Mutagenic Contexts

716 Mutations were divided into four categories: synonymous vs non-synonymous
717 substitutions and high vs low frequency of independent occurrence. For example,
718 consider codon X with 3 non-synonymous substitutions gat->ggt and 1 non-synonymous
719 substitution gat->cgt. In this context, a non-synonymous nucleotide substitution a->g of
720 frequency 4 would be recorded in nucleotide (X-1)*3+2. The low vs high frequency
721 threshold was determined by the 90th percentile of the synonymous mutation frequency
722 distribution (operationally 7). For each mutation, the trinucleotide contexts from the
723 ancestral reconstruction at the nodes where the mutation occurred were compared to
724 the background genome-wide frequencies, computed for the inferred common ancestor
725 of SARS-CoV-2.

726

727 The expected frequencies of the trinucleotides using the background distribution were
728 tabulated; the Yates correction (+/-0.5 to the original count depending on whether the
729 count is below or above the expectation) was applied to the observed frequencies; the
730 log-odds ratios of the (corrected) observed frequencies to the expectation were
731 computed; and CMDS was applied to the Euclidean distances between the log-odds
732 vectors to embed the points onto a plane (Fig. S4 A.). This analysis was then repeated,
733 this time, distinguishing only between high and low frequency substitutions but not N
734 and S (Fig. S4 B). Finally, the differences in the contexts of high frequency synonymous
735 vs non-synonymous events were considered in the same manner and the chi-square
736 statistics ((observed-expected)^2/expected) were compared with the critical chi-square
737 value (p=0.05/64, df=1, Fig. S4 C.).

738

739 Computation of *dN/dS*

740 For each of the 24 ORFs (splitting orf1ab into 15 segments corresponding to the 15
741 mature proteins, nsp11 and nsp12 combined), 10 reduced alignments were constructed
742 as follows. Sequences were ordered based on diversity, in the same order with which
743 they were included in the constraint trees. The first 10 sequences are conserved across
744 every alignment and the remaining 40 are unique to each alignment. The reference
745 sequence, NC_045512.2, was additionally added to each reduced alignment. PAML(83)
746 was then used to estimate tN, tS, *dN/dS*, N, S, and N/S for each segment and every
747 reduced alignment.

748 Given the global ancestral reconstruction from Fitch traceback, the total number of non-
749 synonymous and synonymous substitutions (nN and nS, respectively) as well as these
750 tallies normalized by the respective segment length (tN, and tS, respectively) were
751 retrieved for each segment. . A hybrid *dN/dS* value for each segment was estimated to
752 be (nN/nS)/(N/S)* where (N/S)* is the median value of N/S across all repeats for the
753 segment.

754

Metadata Assignment

Headers for all isolates belonging to CD-HIT clusters with a representative incorporated into the alignment with fewer than 10 interior ambiguous characters were processed to extract the sequencing date and location. Sequencing location abbreviations were matched to full names and the latitude/longitude of a representative city for each location was retrieved from simplemaps (https://simplemaps.com/data/world-cities)(84).

Regional Divergence Analysis

Two approaches, one partition dependent and one partition independent, were used as described in the main text. The Hellinger distance between regions over a sliding time window was computed between regions for the 11 (partitions/variant clades) group distribution. Next, 400 isolates were randomly selected from each region over a sliding window and 200 pairs within each region as well as 200 pairs between each pair of regions were composed. The tree distance between each pair was computed and the mean for each inter- and intra-regional pair tree-distance distribution was recorded. In Figs. 3C and S16, the 25th, 50th, and 75th percentiles are shown of the 15 possible pairs of (6) regions. Regions are selected based on GISAID metadata. The inter-regional tree divergence (Figs. 3C, top and S16C) is reported as the ratio between the mean of the inter-regional pair tree-distance and the mean of the intra-regional pair tree distances across both regions.

775 ## Figure legends

776

777 **Figure 1. Evolution of SARS-CoV-2.**

778 **A.** Global tree reconstruction with 8 principal partitions and 3 variant clades enumerated
779 and color-coded. **B.** Signatures of amino acid replacements for each partition. Sites are
780 ordered as they appear in the genome. The proteins along with nucleotide and amino
781 acid numbers are indicated underneath each column. **C.** Site history trees for spike 614
782 and nucleocapsid 203 positions. Nodes were included in this reduced tree based on the
783 following criteria: those immediately succeeding a substitution; representing the last
784 common ancestor of at least two substitutions; or terminal nodes representing branches
785 of five sequences or more (approximately, based on tree weight). Edges are colored
786 according to their position in the main partitions and the line type corresponds to the
787 target mutation (solid) or any other state (dashed). Synonymous mutations are not
788 shown. These sites are largely binary as are most sites in the genome. The sizes of the
789 terminal node sizes are proportional to the log of the weight descendent from that node
790 beyond which no substitutions in the site occurred. Node color corresponds to target
791 mutation (black) or any other state (gray). **D.** Network of putative epistatic interactions
792 for likely positively selected residues in the N and S proteins.

793

794 **Figure 2. Regional SARS-CoV-2 partition dynamics during the COVID-19**
795 **pandemic.** Probability distributions shown, for the absolute number of sequences, see
796 Fig. S15.

797

798 **Figure 3. Global and regional trends in SARS-CoV-2 evolution. A.** Global
799 distribution of sequences with sequencing locations in each of the six regions
800 considered. Color scheme is for visual distinction only. **B.** Intra-regional diversity
801 measured by the mean tree-distance for pairs of isolates. **C.** (Top) The Hellinger
802 distance for all pairs of regions over the 11 partition/clade distribution. 25th, 50th, 75th
803 percentiles shown. (Bottom) The ratio of the mean tree-distance for pairs of isolates
804 between regions vs. isolates within regions. 25th, 50th, 75th percentiles shown. **D.** The
805 frequency of S|614G, at least one NLS-associated variant (N|194L, N119L, N203K,

806 N205I, and N220V), and at least one emerging spike variant (Fig. S23, excluding
807 S|477N).

Supplemental Figures

Figure S1. 25th, median (solid line), and 75th percentiles of the silhouette score distribution for 100 stochastically initiated rounds of k-means clustering for 2-16 clusters and a projection of the 3D embedding of the pairwise Hamming distance matrix between SARC-CoV-2 genomes. Partitions are color-coded and wires enclose the convex hulls for each of the five optimal clusters.

Figure S2. A. Distributions of the moving average, respecting segment boundaries, across a 100 codon window for synonymous (blue) and amino acid (orange) substitutions. Solid lines: normal approximations of the distributions (same median and interquartile distance); solid lines: approximation with the same median and theoretical (Poisson) variance. **B.** Moving averages, respecting segment boundaries, across a 100 codon window for synonymous and nonsynonymous substitutions per site, raw (top) and normalized by the median (bottom). There are several regions in the genome with an apparent dramatic excess of synonymous substitutions: 5' end of orf1ab gene; most of the M gene; 3'-half of the N gene, as well as amino acid substitutions: most of the orf3a gene; most of the orf7a gene; most of the orf8 gene; and several regions in of the N gene.

Figure S3. Moving average over a window of 1000 codons, not respecting segment boundaries, of the total number of nucleotide exchanges n1->n2 summed over all substitutions. The ratio to the median over the entire alignment is also displayed as well as the normalized exchange distribution *(i.e.* #c->t/(#c->t+#c->g+#c->a)).

Figure S4 A. Two dimensional embedding of the Euclidean distances between the log-odds vectors of low and high frequency, nonsynonymous and synonymous mutations in the space of trinucleotide contexts relative to background expectation. The context of the high-frequency events (both S and N) is dramatically different from the background frequencies. There is a strong common component in the deviation of both kinds of high-frequency events. The context of the low-frequency events (both S and N) also differs slightly, in the same direction, from the background frequencies. There is a consistent distinction between synonymous and non-synonymous events, suggesting that a single mutagenic context or mechanistic bias does not account for both S and N events. **B.** Log odds ratio of low and high frequency mutations, both synonymous and nonsynonymous, relative to background expectation for each trinucleotide context. The NCN context (i.e. all mutations C->D) harbors dramatically more mutation events than the other contexts (all 16 NCN events are within the top 20 most-biased high-frequency events). The log-odds ratios for low-frequency events are poorly correlated with those

847 for high-frequency events, suggesting that different mechanisms may be responsible for
848 the strong bias observed among high frequency events and the weaker bias observed
849 among low frequency events. **C.** Log odds ratio of high frequency nonsynonymous
850 mutations relative to the background expectation from the sum of both high
851 synonymous and high nonsynonymous mutations vs. the sum + 1. There are 20
852 contexts where synonymous and non-synonymous events differ significantly (chi-sq>
853 11.28). 2/9 contexts with an excess of non-synonymous events are NCN (gct,tct). The
854 remaining 7 are NGN (agt,gga,aga,ggt,agc,tgt). This additionally suggests that these
855 non-synonymous events could be driven by other mechanisms. There is no correlation
856 between the frequency of event context and the log-odds ratio for non-synonymous
857 events, further suggesting that the log-odds ratio is not biased by hot-spot mutation
858 context.

859

860 **Figure S5.** Correspondence between the "tree length for dN", "tree length for dS", and
861 *dN/dS* between PAML and the results of the ancestral reconstruction utilizing Fitch
862 traceback across 24 ORFs. Three high outliers in the PAML tS distribution are identified
863 in the third plot and omitted from the first two.

864

865 **Figure S6. A.** The number of nonsynonymous events vs the number of synonymous
866 events per codon. **B.** The moving average of 100 codons, respecting segment
867 boundaries. **C.** The moving average after removing outlier high frequency events. Rho
868 refers to Spearman. Dashed lines are 2/1.3*x reflecting the genome-wide ratio of
869 nonsynonymous to synonymous substitutions, solid lines are linear best fit. Red points
870 correspond to the middle third of the N protein.

871

872 **Figure S7.** Moving averages across a 100 codon window for synonymous and
873 nonsynonymous substitutions per site in the N protein after removing outlier high
874 frequency events. The nonsynonymous substitution frequencies in the center of the
875 protein are not elevated relative to either terminus.

876

877 **Figure S8.** The fraction of sites with at least one substitution vs moving averages,
878 respecting segment boundaries, over windows of 100 codons for synonymous and
879 nonsynonymous substitutions.

880

881 **Figure S9.** Site history trees for spike 69 as drawn in Fig. 1C.

882

Figure S10. Epistatic network for the tree including mutations with NCN context and meeting all other criteria for positive selection. Mutations in the polyprotein are not displayed.

Figures S11. Correlation between sequencing date and tree distance to the root for all isolates with metadata as well as those which appear explicitly in the tree.

Figures S12-14. Global distribution of sequences. Color represents the number of sequences from that location and size represents the fraction of sequences from the clade displayed. Partition indices are in the top left corner of each map.

Figure S15. Regional SARS-CoV-2 partition dynamics during the COVID-19 pandemic (absolute number of sequences shown in contrast to Fig. 2).

Figure S16. The mean tree distance between pairs of isolates **A.** from different regions, **B.** within the same region (averaged over both regions in each pair) and **C.** The ratio over time (see Methods). 25th, 50th, and 75th percentiles of all 15 pairs of 6 regions. The ratio reported is between the mean of the inter-regional pair tree-distance and the mean of the intra-regional pair tree distances across both regions for each pair of regions.

Figure S17. Regional distributions of major partitions in the global topology March vs. July and July vs. November.

Figure S18. The frequencies of NLS-associated mutations N|194L, N119L, N203K, N205I, and N220V over time and across geographic regions along with S|614G for reference.

Figure S19. The Kullback-Leibler divergence and sequence logo for the 15 most divergent codons in sequences sourced after October 15, 2020 from Oceania in partition 7 vs. all sequences from Oceania in partition 7.

Figure S20. The Kullback-Leibler divergence and sequence logo for the 15 most divergent codons in sequences sourced after November 1, 2020 from Oceania in partition 6 vs. all sequences from Oceania in partition 6.

Figure S21. The Kullback-Leibler divergence and sequence logo for the 15 most divergent codons in sequences sourced after November 1, 2020 from Africa in partition 6 vs. all sequences from Africa in partition 6.

Figures S22-24. The frequencies of variant-associated mutations in the spike protein over time and geographic regions.

Figure S25. Regional SARS-CoV-2 variant clade dynamics during the COVID-19 pandemic (log of absolute number of sequences shown).

Supplemental Tables

Table S1. The list of all mutations either in the top 100 most commonly observed or top 100 with the greatest number of parallel substitutions ordered as they appear in the genome.

Table S2. List of sites most likely to be evolving under positive selection. For List 2 the average tree fraction descendant from each candidate positively selected amino acid replacement must be sufficiently large(see Methods).

Table S3. All epistatic interactions among states meeting the criteria outlined in the main text for likely positive selection with binomial/Poisson scores greater than 5 or at least 2 simultaneous substitutions. Each mutation must have a minimum weight of approximately 200 leaves and each pair, 100 leaves. Each pair is arbitrarily ordered and the numbers of simultaneous, descendant, and independent substitutions are tabulated.

Table S4. List 1. List of variant mutations and variant IDs sorted by the number of variant ID's assigned to each mutation. **List 2**. List of all pairs of mutations associated with a single variant ID (internal variant ID's excluded. **List 3**. List of putative epistatic interactions between variant mutations and other states in the tree.

949 **Table S5.** The number of isolates (out of approximately 175k) observed to bear at least
950 one substitution relative to the reference sequence, NC_045512.2, within the regions
951 specified. These regions are commonly used within PCR assays for diagnostic testing.

952

953

954

955 1. Drake JW & Holland JJ (1999) Mutation rates among RNA viruses. *Proceedings of the National*
956 *Academy of Sciences* 96(24):13910-13913.
957 2. Sanjuán R (2012) From molecular genetics to phylodynamics: evolutionary relevance of
958 mutation rates across viruses. *PLoS Pathog* 8(5):e1002685.
959 3. Simmonds P, Aiewsakun P, & Katzourakis A (2019) Prisoners of war - host adaptation and its
960 constraints on virus evolution. *Nat Rev Microbiol* 17(5):321-328.
961 4. Elena SF & Sanjuán R (2005) Adaptive value of high mutation rates of RNA viruses: separating
962 causes from consequences. *J Virol* 79(18):11555-11558.
963 5. Wertheim JO & Kosakovsky Pond SL (2011) Purifying selection can obscure the ancient age of
964 viral lineages. *Molecular biology and evolution* 28(12):3355-3365.
965 6. Jenkins GM, Rambaut A, Pybus OG, & Holmes EC (2002) Rates of molecular evolution in RNA
966 viruses: a quantitative phylogenetic analysis. *Journal of molecular evolution* 54(2):156-165.
967 7. Holmes EC (2003) Patterns of intra-and interhost nonsynonymous variation reveal strong
968 purifying selection in dengue virus. *Journal of virology* 77(20):11296-11298.
969 8. Jerzak G, Bernard KA, Kramer LD, & Ebel GD (2005) Genetic variation in West Nile virus from
970 naturally infected mosquitoes and birds suggests quasispecies structure and strong purifying
971 selection. *The Journal of general virology* 86(Pt 8):2175.
972 9. Wolf YI, Viboud C, Holmes EC, Koonin EV, & Lipman DJ (2006) Long intervals of stasis punctuated
973 by bursts of positive selection in the seasonal evolution of influenza A virus. *Biology direct*
974 1(1):1-19.
975 10. Bush RM, Bender CA, Subbarao K, Cox NJ, & Fitch WM (1999) Predicting the evolution of human
976 influenza A. *Science* 286(5446):1921-1925.
977 11. Bush RM, Fitch WM, Bender CA, & Cox NJ (1999) Positive selection on the H3 hemagglutinin
978 gene of human influenza virus A. *Molecular biology and evolution* 16(11):1457-1465.
979 12. Koirala A, Joo YJ, Khatami A, Chiu C, & Britton PN (2020) Vaccines for COVID-19: The current
980 state of play. *Paediatric respiratory reviews* 35:43-49.
981 13. Benson DA*, et al.* (2012) GenBank. *Nucleic acids research* 41(D1):D36-D42.
982 14. Elbe S & Buckland-Merrett G (2017) Data, disease and diplomacy: GISAID's innovative
983 contribution to global health. *Global Challenges* 1(1):33-46.
984 15. Zhao W-M*, et al.* (2020) The 2019 novel coronavirus resource. *Yi chuan= Hereditas* 42(2):212-
985 221.
986 16. Lanfear R (A global phylogeny of SARS-CoV-2 from GISAID data, including sequences deposited
987 up to 31-July-2020. 2020. *Zenodo*.
988 17. Morel B*, et al.* (2020) Phylogenetic analysis of SARS-CoV-2 data is difficult. *bioRxiv*.
989 18. Fitch WM (1971) Toward defining the course of evolution: minimum change for a specific tree
990 topology. *Systematic Biology* 20(4):406-416.
991 19. Kumar S*, et al.* (2020) An evolutionary portrait of the progenitor SARS-CoV-2 and its dominant
992 offshoots in COVID-19 pandemic. *bioRxiv*.

20. Forster P, Forster L, Renfrew C, & Forster M (2020) Phylogenetic network analysis of SARS-CoV-2 genomes. *Proceedings of the National Academy of Sciences* 117(17):9241-9243.
21. Fountain-Jones NM*, et al.* (2020) Emerging phylogenetic structure of the SARS-CoV-2 pandemic. *Virus evolution* 6(2):veaa082.
22. Mavian C*, et al.* (2020) Sampling bias and incorrect rooting make phylogenetic network tracing of SARS-COV-2 infections unreliable. *Proceedings of the National Academy of Sciences* 117(23):12522-12523.
23. Sánchez-Pacheco SJ, Kong S, Pulido-Santacruz P, Murphy RW, & Kubatko L (2020) Median-joining network analysis of SARS-CoV-2 genomes is neither phylogenetic nor evolutionary. *Proceedings of the National Academy of Sciences* 117(23):12518-12519.
24. Pipes L, Wang H, Huelsenbeck J, & Nielsen R (2020) Assessing uncertainty in the rooting of the SARS-CoV-2 phylogeny. *bioRxiv*.
25. van Dorp L*, et al.* (2020) Emergence of genomic diversity and recurrent mutations in SARS-CoV-2. *Infection, Genetics and Evolution* 83:104351.
26. Timani KA*, et al.* (2005) Nuclear/nucleolar localization properties of C-terminal nucleocapsid protein of SARS coronavirus. *Virus research* 114(1-2):23-34.
27. Goldman N & Yang Z (1994) A codon-based model of nucleotide substitution for protein-coding DNA sequences. *Molecular biology and evolution* 11(5):725-736.
28. Richard D, Owen CJ, van Dorp L, & Balloux F (2020) No detectable signal for ongoing genetic recombination in SARS-CoV-2. *bioRxiv*:2020.2012.2015.422866.
29. Ye ZW*, et al.* (2020) Zoonotic origins of human coronaviruses. *Int J Biol Sci* 16(10):1686-1697.
30. Li X*, et al.* (2020) Emergence of SARS-CoV-2 through recombination and strong purifying selection. *Sci Adv* 6(27).
31. Zhu Z, Meng K, & Meng G (2020) Genomic recombination events may reveal the evolution of coronavirus and the origin of SARS-CoV-2. *Sci Rep* 10(1):21617.
32. Ji W, Wang W, Zhao X, Zai J, & Li X (2020) Cross-species transmission of the newly identified coronavirus 2019-nCoV. *J Med Virol* 92(4):433-440.
33. Graham RL & Baric RS (2010) Recombination, reservoirs, and the modular spike: mechanisms of coronavirus cross-species transmission. *J Virol* 84(7):3134-3146.
34. Bobay LM, O'Donnell AC, & Ochman H (2020) Recombination events are concentrated in the spike protein region of Betacoronaviruses. *PLoS Genet* 16(12):e1009272.
35. Rochman ND, Wolf YI, & Koonin EV (2020) Deep phylogeny of cancer drivers and compensatory mutations. *Communications biology* 3(1):1-11.
36. Korber B*, et al.* (2020) Tracking changes in SARS-CoV-2 Spike: evidence that D614G increases infectivity of the COVID-19 virus. *Cell* 182(4):812-827. e819.
37. Volz E*, et al.* (2021) Evaluating the effects of SARS-CoV-2 Spike mutation D614G on transmissibility and pathogenicity. *Cell* 184(1):64-75. e11.
38. Breen MS, Kemena C, Vlasov PK, Notredame C, & Kondrashov FA (2012) Epistasis as the primary factor in molecular evolution. *Nature* 490(7421):535-538.
39. Starr TN & Thornton JW (2016) Epistasis in protein evolution. *Protein Sci* 25(7):1204-1218.
40. Phillips PC (2008) Epistasis--the essential role of gene interactions in the structure and evolution of genetic systems. *Nat Rev Genet* 9(11):855-867.
41. Domingo J, Baeza-Centurion P, & Lehner B (2019) The Causes and Consequences of Genetic Interactions (Epistasis). *Annu Rev Genomics Hum Genet* 20:433-460.
42. Faria NR*, et al.* (2021) Genomic characterisation of an emergent SARS-CoV-2 lineage in Manaus: preliminary findings. *January* 12:2021.

1039 43. Tegally H*, et al.* (2020) Emergence and rapid spread of a new severe acute respiratory
1040 syndrome-related coronavirus 2 (SARS-CoV-2) lineage with multiple spike mutations in South
1041 Africa. *medRxiv*.
1042 44. Voloch CM*, et al.* (2020) Genomic characterization of a novel SARS-CoV-2 lineage from Rio de
1043 Janeiro, Brazil. *medRxiv*.
1044 45. Zhang W*, et al.* (2021) Emergence of a Novel SARS-CoV-2 Variant in Southern California. *JAMA*.
1045 46. England PH (Variants: distribution of cases data.
1046 47. Brejová B*, et al.* (2021) B. 1.258_Delta, a SARS-CoV-2 variant with Delta_H69, Delta_V70 in the
1047 Spike protein circulating in the Czech Republic and Slovakia. *arXiv preprint arXiv:2102.04689*.
1048 48. Statens Serum Institut (2020) Mutations in the mink virus.
1049 https://www.ssi.dk/aktuelt/nyheder/2020/mutationer-i-minkvirus
1050 49. Munnink BBO*, et al.* (2021) Transmission of SARS-CoV-2 on mink farms between humans and
1051 mink and back to humans. *Science* 371(6525):172-177.
1052 50. Li Q*, et al.* (2020) The impact of mutations in SARS-CoV-2 spike on viral infectivity and
1053 antigenicity. *Cell* 182(5):1284-1294. e1289.
1054 51. Wibmer CK*, et al.* (2021) SARS-CoV-2 501Y. V2 escapes neutralization by South African COVID-19
1055 donor plasma. *BioRxiv*.
1056 52. Fiorentini S*, et al.* (2021) First detection of SARS-CoV-2 spike protein N501 mutation in Italy in
1057 August, 2020. *The Lancet. Infectious Diseases*.
1058 53. van Dorp L*, et al.* (2020) Recurrent mutations in SARS-CoV-2 genomes isolated from mink point
1059 to rapid host-adaptation. *bioRxiv*.
1060 54. Thomson EC*, et al.* (2020) The circulating SARS-CoV-2 spike variant N439K maintains fitness
1061 while evading antibody-mediated immunity. *bioRxiv*.
1062 55. Rochman ND, Wolf YI, & Koonin EV (2020) Substantial Impact of Post Vaccination Contacts on
1063 Cumulative Infections during Viral Epidemics. *medRxiv*.
1064 56. Gandon S & Day T (2007) The evolutionary epidemiology of vaccination. *Journal of the Royal*
1065 *Society Interface* 4(16):803-817.
1066 57. Brueggemann AB, Pai R, Crook DW, & Beall B (2007) Vaccine escape recombinants emerge after
1067 pneumococcal vaccination in the United States. *PLoS Pathog* 3(11):e168.
1068 58. Scherer A & McLean A (2002) Mathematical models of vaccination. *British Medical Bulletin*
1069 62(1):187-199.
1070 59. Geoghegan JL & Holmes EC (2018) The phylogenomics of evolving virus virulence. *Nature*
1071 *Reviews Genetics* 19(12):756-769.
1072 60. Cressler CE, McLeod DV, Rozins C, Van Den Hoogen J, & Day T (2016) The adaptive evolution of
1073 virulence: a review of theoretical predictions and empirical tests. *Parasitology* 143(7):915-930.
1074 61. Rochman ND, Wolf YI, & Koonin EV (2020) Evolution of Human Respiratory Virus Epidemics.
1075 *medRxiv*.
1076 62. Gussow AB*, et al.* (2020) Genomic determinants of pathogenicity in SARS-CoV-2 and other
1077 human coronaviruses. *Proceedings of the National Academy of Sciences* 117(26):15193-15199.
1078 63. Hodcroft EB*, et al.* (2020) Emergence and spread of a SARS-CoV-2 variant through Europe in the
1079 summer of 2020. *MedRxiv*.
1080 64. Zhang Y*, et al.* (2020) The ORF8 protein of SARS-CoV-2 mediates immune evasion through
1081 potently downregulating MHC-I. *biorxiv*.
1082 65. Zinzula L (2020) Lost in deletion: The enigmatic ORF8 protein of SARS-CoV-2. *Biochemical and*
1083 *Biophysical Research Communications*.
1084 66. Gong LI, Suchard MA, & Bloom JD (2013) Stability-mediated epistasis constrains the evolution of
1085 an influenza protein. *Elife* 2:e00631.

1086 67. Sanjuán R, Cuevas JM, Moya A, & Elena SF (2005) Epistasis and the adaptability of an RNA virus.
1087 *Genetics* 170(3):1001-1008.
1088 68. Lyons DM & Lauring AS (2018) Mutation and Epistasis in Influenza Virus Evolution. *Viruses* 10(8).
1089 69. Kryazhimskiy S, Dushoff J, Bazykin GA, & Plotkin JB (2011) Prevalence of epistasis in the
1090 evolution of influenza A surface proteins. *PLoS Genet* 7(2):e1001301.
1091 70. Kuipers J*, et al.* (2020) Within-patient genetic diversity of SARS-CoV-2. *BioRxiv*.
1092 71. Rose R*, et al.* (2020) Intra-host site-specific polymorphisms of SARS-CoV-2 is consistent across
1093 multiple samples and methodologies. *medRxiv*:2020.2004.2024.20078691.
1094 72. Armero A, Berthet N, & Avarre JC (2021) Intra-Host Diversity of SARS-Cov-2 Should Not Be
1095 Neglected: Case of the State of Victoria, Australia. *Viruses* 13(1).
1096 73. Artesi M*, et al.* (2020) A recurrent mutation at position 26340 of SARS-CoV-2 is associated with
1097 failure of the E gene quantitative reverse transcription-PCR utilized in a commercial dual-target
1098 diagnostic assay. *Journal of clinical microbiology* 58(10).
1099 74. Ortiz-Prado E, et al. (2020) Clinical, molecular and epidemiological characterization of the SARS-
1100 CoV2 virus and the Coronavirus disease 2019 (COVID-19), a comprehensive literature review.
1101 *Diagnostic microbiology and infectious disease* 115094.
1102 75. Dong Y, et al. (2020) A systematic review of SARS-CoV-2 vaccine candidates. *Signal transduction*
1103 *and targeted therapy* 5.1.
1104 76. Lai S*, et al.* (2020) Assessing the effect of global travel and contact reductions to mitigate the
1105 COVID-19 pandemic and resurgence. *medRxiv*.
1106 77. Fu L, Niu B, Zhu Z, Wu S, & Li W (2012) CD-HIT: accelerated for clustering the next-generation
1107 sequencing data. *Bioinformatics* 28(23):3150-3152.
1108 78. Li W & Godzik A (2006) Cd-hit: a fast program for clustering and comparing large sets of protein
1109 or nucleotide sequences. *Bioinformatics* 22(13):1658-1659.
1110 79. Katoh K, Misawa K, Kuma Ki, & Miyata T (2002) MAFFT: a novel method for rapid multiple
1111 sequence alignment based on fast Fourier transform. *Nucleic acids research* 30(14):3059-3066.
1112 80. Price MN, Dehal PS, & Arkin AP (2010) FastTree 2–approximately maximum-likelihood trees for
1113 large alignments. *PloS one* 5(3):e9490.
1114 81. Nguyen L-T, Schmidt HA, Von Haeseler A, & Minh BQ (2015) IQ-TREE: a fast and effective
1115 stochastic algorithm for estimating maximum-likelihood phylogenies. *Molecular biology and*
1116 *evolution* 32(1):268-274.
1117 82. MathWorks I (1992) *MATLAB, high-performance numeric computation and visualization*
1118 *software: reference guide* (MathWorks).
1119 83. Yang Z (2007) PAML 4: phylogenetic analysis by maximum likelihood. *Molecular biology and*
1120 *evolution* 24(8):1586-1591.
1121 84. Simplemaps. World Cities Database. https://simplemaps.com/data/world-cities

1122

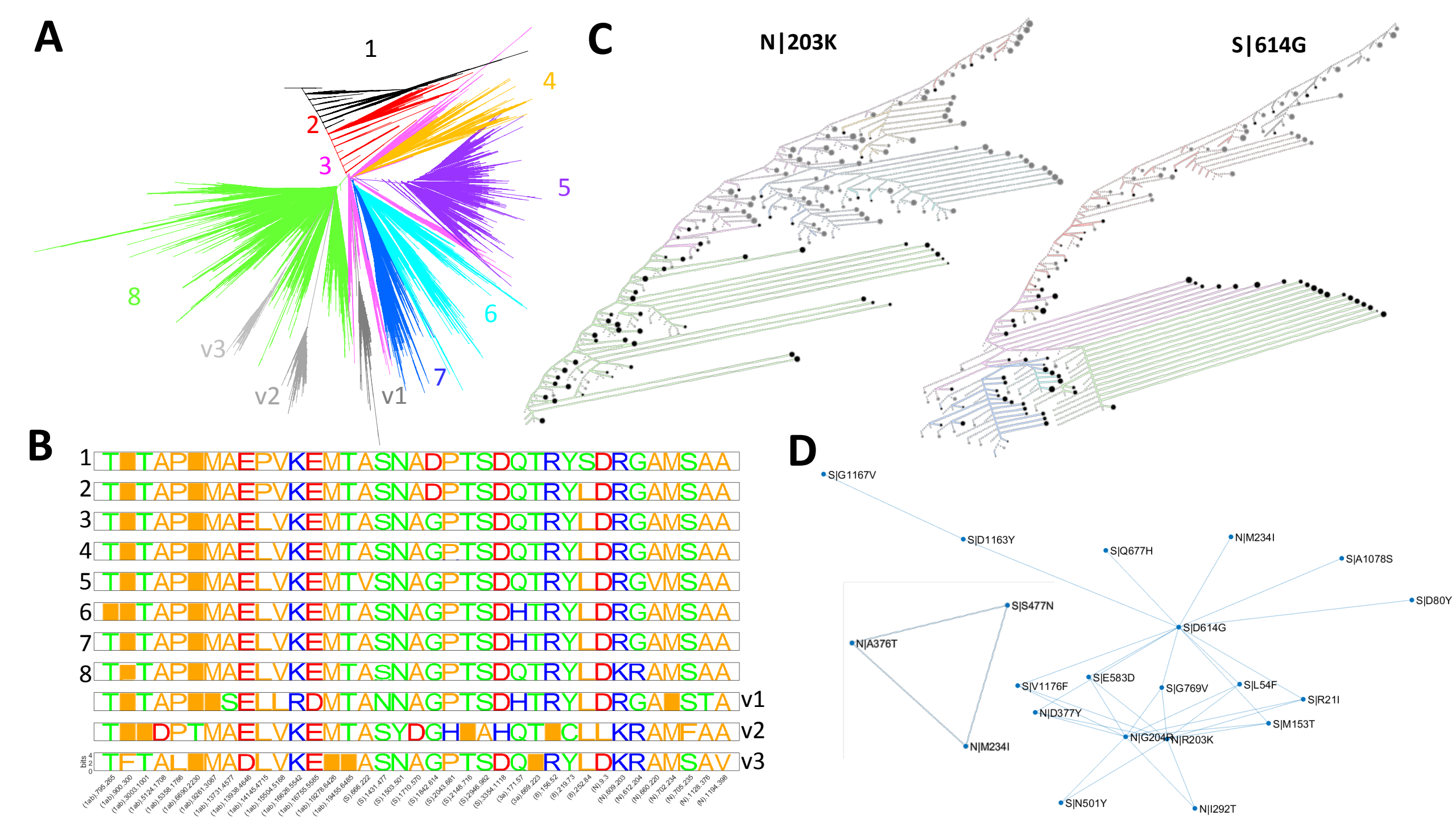
A
1
2
3
4
5
6
7
8
v1
v2
v3
B
1 T■TAP■MAEPVKEMTASNADPTSDQTRYSDRGAMSAA
2 T■TAP■MAEPVKEMTASNADPTSDQTRYLDRGAMSAA
3 T■TAP■MAELVKEMTASNAGPTSDQTRYLDRGAMSAA
4 T■TAP■MAELVKEMTASNAGPTSDQTRYLDRGAMSAA
5 T■TAP■MAELVKEMTVSNAGPTSDQTRYLDRGVMSAA
6 ■■TAP■MAELVKEMTASNAGPTSDHTRYLDRGAMSAA
7 T■TAP■MAELVKEMTASNAGPTSDHTRYLDRGAMSAA
8 T■TAP■MAELVKEMTASNAGPTSDQTRYLDKRAMSAA
v1 T■TAP■■SELLRDMTANNAGPTSDHTRYLDRGA■STA
v2 T■■DPTMAELVKEMTASYDGH■AHQT■CLLKRAMFAA
v3 TFTAL■MADLVKE■■ASNAGPTSDQ■RYLDKRAMSAV
bits
C
N|203K
S|614G
D
S|G1167V
S|D1163Y
S|Q677H
N|M234I
S|A1078S
S|D80Y
S|S477N
S|D614G
N|A376T
S|V1176F
S|E583D
S|G769V
S|L54F
S|R21I
N|D377Y
S|M153T
N|G204R
N|R203K
N|M234I
S|N501Y
N|I292T

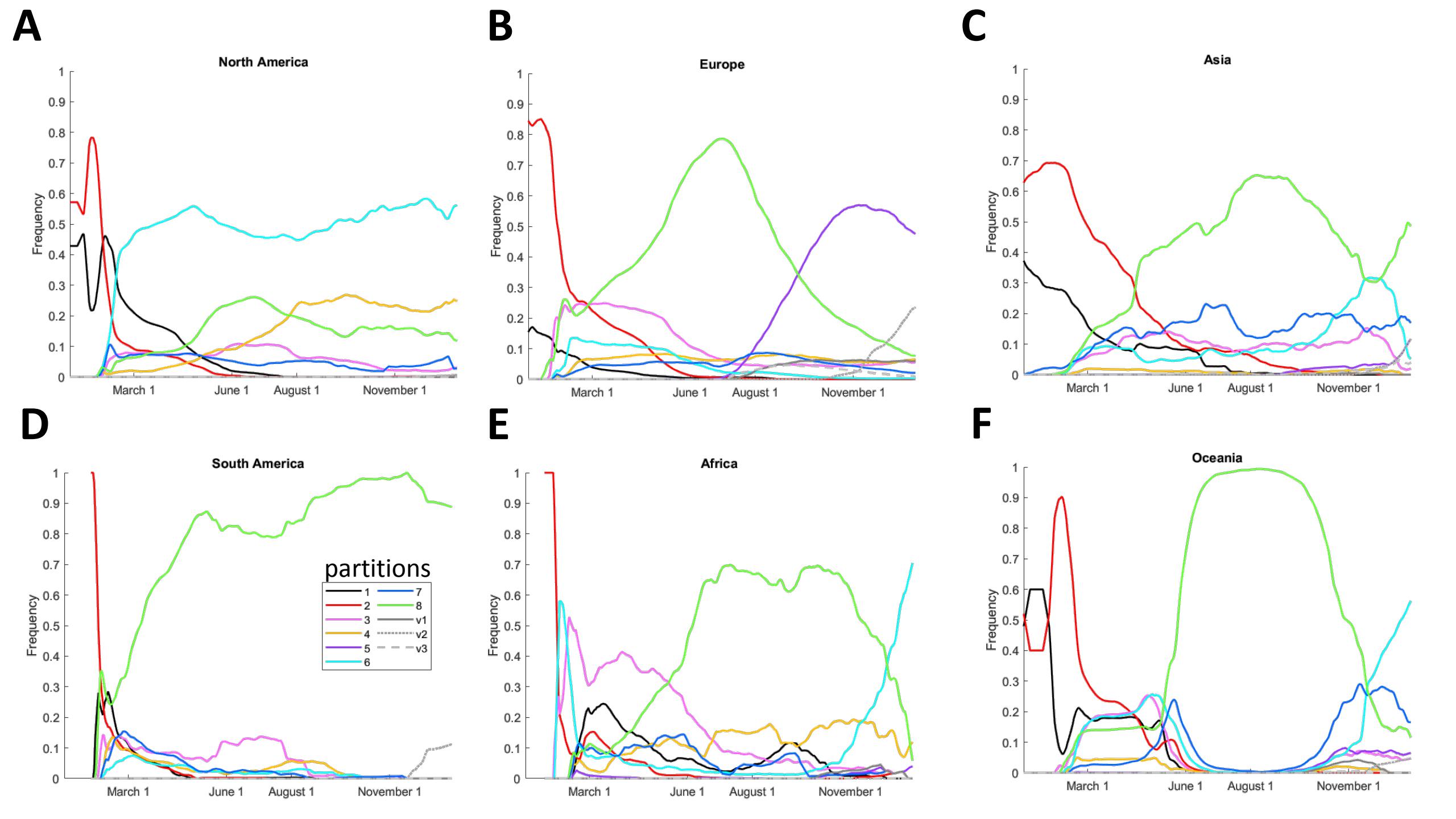
A
North America
B
Europe
C
Asia
D
South America
E
Africa
F
Oceania
Frequency
March 1
June 1
August 1
November 1
partitions
1
2
3
4
5
6
7
8
v1
v2
v3

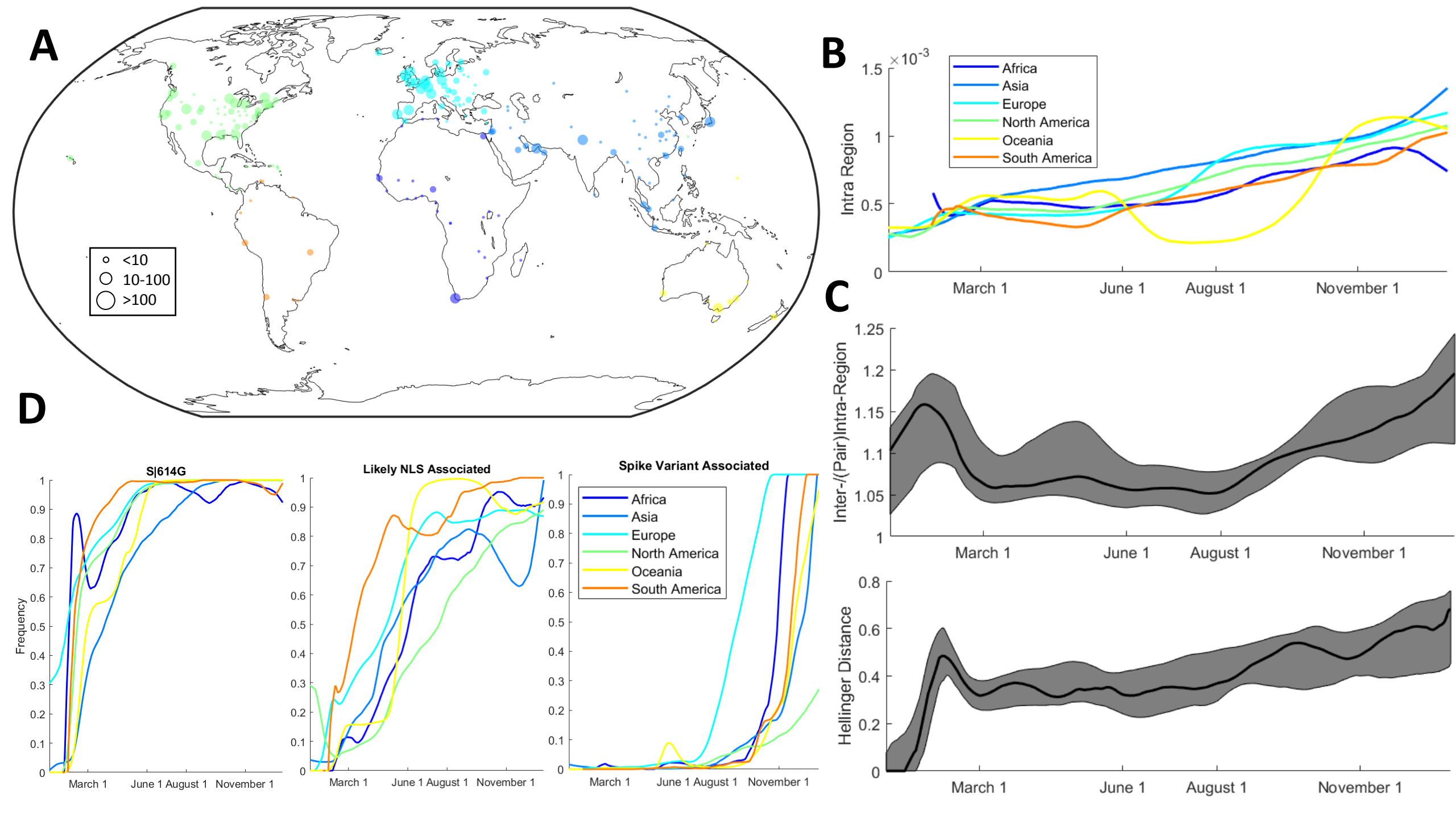
A
<10
10-100
>100
B
×10^-3
Intra Region
Africa
Asia
Europe
North America
Oceania
South America
March 1
June 1
August 1
November 1
C
Inter-/(Pair)Intra-Region
Hellinger Distance
D
S|614G
Likely NLS Associated
Spike Variant Associated
Frequency